Proceedings of SPIE, Vol. 4038, April 2000

Three-Dimensional FDTD Model to Study the Elastic-Wave Interaction with Buried Land Mines

Christoph T. Schröder and Waymond R. Scott, Jr.

School of Electrical and Computer Engineering
Georgia Institute of Technology
Atlanta, GA 30332-0250
USA

ABSTRACT

A three-dimensional finite-difference model for elastic waves in the ground has been developed and implemented. The model is used to investigate the interaction of elastic waves with buried land mines. When elastic waves interact with a buried mine, a strong resonance occurs at the mine location. The resonance can be used to enhance the mine's signature and to distinguish the mine from clutter. Results are presented for a single mine buried in the ground and several mines in the presence of clutter. The predictions of the numerical model are in fairly good agreement with experimental results.

Keywords: land mine detection, elastic, acoustic, FDTD, finite-difference

1. INTRODUCTION

A new technique is being investigated at the Georgia Institute of Technology, in which buried land mines are located by using both elastic (acoustic) and electromagnetic waves in a synergistic manner.[1–3] Here, elastic waves interact with a buried land mine and cause the mine and the surface above the mine to vibrate. An electromagnetic radar records the vibrations and, thus, detects the mine. During the process of developing the elastic/electromagnetic sensor, a major part has been the implementation of a numerical model which simulates the interaction of the elastic waves with the buried land mines.[4]

The numerical model is based on the finite-difference time-domain (FDTD) method. The equation of motion and the stress-strain relation, together with a constitutive relation, form a set of first-order partial differential equations that completely describes the elastic wave motion in a medium. Introducing finite differences, this set of equations can be discretized and adapted to the finite-difference time-domain modeling scheme. Assuming that the field is known at one initial time t_0, this numerical scheme is used to determine the field values at later times $t > t_0$.

The finite-difference model has been implemented in two and three dimensions. The solution space is discretized and a staggered finite-difference grid is introduced. The grid is surrounded by a perfectly matched layer, that absorbs the outward traveling waves and, thus, models the infinite extend of the solution space. The finite-difference model has been implemented in a fully parallel fashion. The computations for this paper's results have been performed both on a Cray T3E parallel supercomputer located at the ERDC Massively Shared Resource Center in Vicksburg, Mississppi, and on a Beowulf PC cluster located at the Georgia Institute of Technology. The Beowulf cluster has been developed and built especially for the model described in this paper.

The numerical model has been very helpful for explaining and understanding the experimental results. The numerical model bears several advantages over the experimental model. With the numerical model, it is possible to visualize the elastic wave motion within the ground, whereas with the experimental model only the wave fields on the surface can be observed. Furthermore, no noise is present in the numerical model, and material parameters can be adjusted easily.

Electronic Mail and Telephone: christoph.schroeder@ee.gatech.edu, 404-894-3123, waymond.scott@ee.gatech.edu, 404-894-3048

Results obtained with the three-dimensional model are presented in this paper. In Sec. 3.1, the propagation of a Rayleigh surface wave is shown as measured experimentally and computed numerically. The surface wave is seen to disperse as it propagates along the surface. The same effect can be also modeled numerically. In Sec. 3.2, the interaction of elastic waves with a buried anti-personnel mine is shown. In both experiment and numerical model, a strong resonance is observed at the mine location. Finally, in Sec. 3.3, the interaction of elastic waves with several buried mines in the presence of clutter is described.

2. THREE-DIMENSIONAL NUMERICAL MODEL

In a realistic setting, one or several mines are buried in the ground, surrounded and covered by various kinds of clutter. To approximate these conditions, experiments have been performed with mines buried in a large sand box.[1] In these experiments, elastic waves are launched by an electrodynamic transducer placed on the surface of the ground. The waves propagate along the surface and interact with the buried land mines. To study these mine-wave interactions, a three-dimensional finite-difference model has been developed.

2.1. Finite-Difference Model

Figure 1 shows the three-dimensional finite-difference model. To reasonably simplify the model, the ground is assumed to be linear, isotropic and lossless. The surface of the ground is modeled as a free-surface, a *Perfectly Matched Layer* terminates the solution space at the remaining grid edges and absorbs the outward traveling waves. The solution space is discretized using a staggered finite-difference grid.[5]

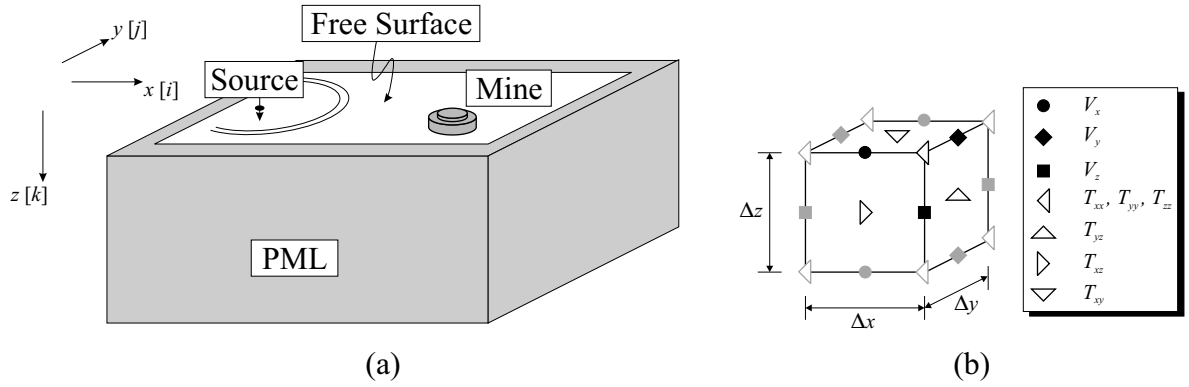

Figure 1. Three-dimensional finite-difference model; (a) lay-out, (b) finite-difference cell.

The elastic wave motion in solids is described by a set of fundamental partial-differential equations: the equation of motion relating the particle velocity vector and the mechanic stress tensor, the strain-velocity relation and the elastic constitutive relation. Combining these equations, a first-order system of equations is obtained describing the elastic wave fields entirely in terms of the particle velocity and the mechanic stress. In three dimensions, three unknown velocity components and six unknown stress tensor components arise.

For the numerical finite-difference model, the derivatives of the partial differential equations are approximated by finite-differences. The finite-difference algorithm shall be explained by deriving the update equations for the x-component of the particle velocity, v_x, (from the first component of the equation of motion) and for the longitudinal stress component, τ_{xx} (from the combined strain-velocity and constitutive relation). Update equations for the other field components can be derived in a similar manner.

The first-order system of equations consists of nine linear independent equations for the three unknown velocity vector components v_x, v_y and v_z, and the six stress tensor components τ_{xx}, τ_{yy}, τ_{zz}, τ_{yz}, τ_{xz} and τ_{xy}. The equations can be written out as

$$\rho \frac{\partial v_x}{\partial t} = \frac{\partial \tau_{xx}}{\partial x} + \frac{\partial \tau_{xy}}{\partial y} + \frac{\partial \tau_{xz}}{\partial z} \tag{1}$$

$$\rho \frac{\partial v_y}{\partial t} = \frac{\partial \tau_{xy}}{\partial x} + \frac{\partial \tau_{yy}}{\partial y} + \frac{\partial \tau_{yz}}{\partial z} \tag{2}$$

$$\rho\frac{\partial v_z}{\partial t} = \frac{\partial \tau_{xz}}{\partial x} + \frac{\partial \tau_{xz}}{\partial y} + \frac{\partial \tau_{zz}}{\partial z} \tag{3}$$

$$\frac{\partial \tau_{xx}}{\partial t} = (\lambda + 2\mu)\frac{\partial v_x}{\partial x} + \lambda\frac{\partial v_y}{\partial y} + \lambda\frac{\partial v_z}{\partial z} \tag{4}$$

$$\frac{\partial \tau_{yy}}{\partial t} = \lambda\frac{\partial v_x}{\partial x} + (\lambda + 2\mu)\frac{\partial v_y}{\partial y} + \lambda\frac{\partial v_z}{\partial z} \tag{5}$$

$$\frac{\partial \tau_{zz}}{\partial t} = \lambda\frac{\partial v_x}{\partial x} + \lambda\frac{\partial v_y}{\partial y} + (\lambda + 2\mu)\frac{\partial v_z}{\partial z} \tag{6}$$

$$\frac{\partial \tau_{yz}}{\partial t} = \mu(\frac{\partial v_y}{\partial z} + \frac{\partial v_z}{\partial y}) \tag{7}$$

$$\frac{\partial \tau_{xz}}{\partial t} = \mu(\frac{\partial v_x}{\partial z} + \frac{\partial v_z}{\partial x}) \tag{8}$$

$$\frac{\partial \tau_{xy}}{\partial t} = \mu(\frac{\partial v_x}{\partial y} + \frac{\partial v_y}{\partial x}), \tag{9}$$

where λ and μ are *Lame's constants* and describe the isotropic solid, and ρ is the material density of the medium.

Taking Eq. (1) and Eq. (4), the update equations for the particle velocity v_x and the longitudinal stress τ_{xx} are derived. Introducing finite-differences in space and time, the partial-differential equations are discretized:

$$\begin{aligned}
&\rho\frac{V_x^{l+0.5}(i,j-0.5,k-0.5) - V_x^{l-0.5}(i,j-0.5,k-0.5)}{\Delta t} = \\
&\quad\frac{T_{xx}^{l}(i+0.5,j-0.5,k-0.5) - T_{xx}^{l}(i-0.5,j-0.5,k-0.5)}{\Delta x} + \frac{T_{xy}^{l}(i,j,k-0.5) - T_{xx}^{l}(i,j-1,k-0.5)}{\Delta y} \\
&\quad+ \frac{T_{xz}^{l}(i,j-0.5,k) - T_{xz}^{l}(i,j-0.5,k-1)}{\Delta z},
\end{aligned} \tag{10}$$

$$\begin{aligned}
&\frac{T_{xx}^{l+1}(i+0.5,j-0.5,k-0.5) - T_{xx}^{l}(i+0.5,j-0.5,k-0.5)}{\Delta t} = \\
&\quad(\lambda+2\mu)\frac{V_x^{l+0.5}(i+1,j-0.5,k-0.5) - V_x^{l+0.5}(i,j-0.5,k-0.5)}{\Delta x} \\
&\quad+\lambda\frac{V_y^{l+0.5}(i+0.5,j,k-0.5) - V_y^{l+0.5}(i+0.5,j-1,k-0.5)}{\Delta y} \\
&\quad+\lambda\frac{V_z^{l+0.5}(i+0.5,j-0.5,k) - V_z^{l+0.5}(i+0.5,j-0.5,k-1)}{\Delta z}.
\end{aligned} \tag{11}$$

Here, the capital letters mark the numerical value of the correspondent field component at a discrete location in space and time. For example, $V_x^{l+0.5}(i,j-0.5,k-0.5)$ stands for the numerical value of the particle velocity v_x at $(x,y,z) = (i\Delta x,(j-0.5)\Delta y,(k-0.5)\Delta z)$ at time $t = (l+0.5)\Delta t$. Knowing $V_x^{l-0.5}$, T_{xx}^{l},T_{xy}^{l} and T_{xz}^{l}, Eq. (10) can be solved for $V_x^{l+0.5}$, i.e. for the particle velocity at the incremented time $t = (l+0.5)\Delta t$:

$$\begin{aligned}
&V_x^{l+0.5}(i,j-0.5,k-0.5) = V_x^{l-0.5}(i,j-0.5,k-0.5)+ \\
&\quad+\frac{\Delta t}{\rho}\left[\frac{T_{xx}^{l}(i+0.5,j-0.5,k-0.5) - T_{xx}^{l}(i-0.5,j-0.5,k-0.5)}{\Delta x} + \frac{T_{xy}^{l}(i,j,k-0.5) - T_{xx}^{l}(i,j-1,k-0.5)}{\Delta y}\right. \\
&\quad\left.+\frac{T_{xz}^{l}(i,j-0.5,k) - T_{xz}^{l}(i,j-0.5,k-1)}{\Delta z}\right].
\end{aligned} \tag{12}$$

Similarly, T_{xx}^{l+1} is obtained from Eq. (11):

$$\begin{aligned}
&T_{xx}^{l+1}(i+0.5,j-0.5,k-0.5) = T_{xx}^{l}(i+0.5,j-0.5,k-0.5)+ \\
&\quad+\Delta t\left[(\lambda+2\mu)\frac{V_x^{l+0.5}(i+1,j-0.5,k-0.5) - V_x^{l+0.5}(i,j-0.5,k-0.5)}{\Delta x}\right. \\
&\quad\left.+\lambda\frac{V_y^{l+0.5}(i+0.5,j,k-0.5) - V_y^{l+0.5}(i+0.5,j-1,k-0.5)}{\Delta y}\right.
\end{aligned}$$

$$+ \lambda \frac{V_z^{l+0.5}(i+0.5, j-0.5, k) - V_z^{l+0.5}(i+0.5, j-0.5, k-1)}{\Delta z} \Bigg] . \quad (13)$$

In the same manner, discrete update equations can be obtained for all field components.[6]

The discretization leads to the characteristic finite-difference grid. In this grid, the field components are staggered in space and time. The finite-difference grid can be thought of as being comprised of basis cells. The three-dimensional basis cell for the elastodynamic case resembles strongly the three-dimensional basis cell for electromagnetic finite-difference modeling, the so-called *Yee*-cell.[7] However, due to the stress being a tensor, more field components are present in the elastodynamic case. Figure 1 (b) shows the three-dimensional finite-difference basis cell. The position of the cell in space is labeled with i in the x-direction, with j in the y-direction and with k in the z-direction. Only the field components in black are assigned to the (i, j, k)-th cell. The other field components belong to adjacent cells and are gray in Fig. 1 (b). Note that the field components are not known at the same points in space and time. The grid is laid out such that each field component is surrounded by the field components it is dependent on. The finite-difference algorithm then works as follows. Knowing the field components at one initial time t_0 throughout the entire grid, the field values for later times can be determined. First, the velocity components on the grid are calculated at the incremented time $t_0 + 0.5\Delta t$ using Eq. (10) for v_x and equivalent equations for v_y and v_z. The stress components at $t_0 + \Delta t$ are determined from the velocity components using Eq. (11) and its equivalences. Then, the velocity components are updated using the stress values, the stress components are computed from the velocity components and so on. In this way, the field values can be determined up to any desired time.

When implementing the finite-difference scheme, boundary conditions have to be treated in a special manner. Three different kinds of boundaries arise: the source, internal boundaries (i.e. boundaries within the medium marked by a change in material properties), and external boundaries (i.e. the grid edges).

In the experimental model, an electrodynamic transducer placed on the surface launches the elastic waves. The transducer foot has the shape of a bar. In the numerical model, the transducer is approximated by exciting the particle velocity component normal to the surface, v_z, on an area equivalent to the area of the foot. The motion of the transducer foot has been measured using accelerometers and resembles closely the shape of a differentiated Gaussian pulse. In the numerical model, a differentiated Gaussian pulse is used as excitation, because the excitation must have a smooth shape to avoid numerical dispersion artifacts. To compare the experimental and numerical results, the transfer function of the numerical model at each point in space is determined and convolved with the excitation of the transducer. In this way, the elastic wave fields due to excitation with the real transducer foot motion are obtained.

The conditions at internal boundaries, i.e. at the interfaces between different media, are usually satisfied implicitly. However, to ensure numerical stability, the material properties have to be averaged for components on the boundary. While the material density ρ, appearing in the equation of motion, is averaged directly, the inverse of Lame's constants, λ and μ from the stress-strain relation, must be averaged.

Four external boundaries arise at the four outer grid edges. At its upper edge, the half-space is bounded by a free surface. Due to the continuity of normal stress, the normal stress components vanish at a free surface. In order to satisfy this condition, an extra row must be inserted into the finite-difference grid one step beyond the free-surface boundary.

In order to model the infinite half-space, all waves that are reaching the three remaining outer grid edges must be perfectly transmitted and absorbed. The boundary condition that does this most accurately is the *Perfectly Matched Layer* (PML) boundary condition, first introduced by Berenger[8] and adapted to elastodynamics by Chew and Liu.[9] Here, a non-physical splitting of the wave fields allows the introduction of a lossy boundary layer that is perfectly matched to the solution space. In continuous space, it has been shown that an arbitrarily polarized wave incident on this PML medium is perfectly transmitted. The wave experiences the exact same phase velocity and wave impedance as in the solution space, while rapidly decaying along the axis normal to the PML-medium interface. In discrete space, however, the PML will not be matched perfectly to the solution space. To keep reflections at the interface small, a tapered loss profile is chosen for the PML.[3]

2.2. Parallelization

The finite-difference model has been implemented in a fully parallel fashion. When implemented on a parallel computer, the three-dimensional finite-difference grid is divided into several sub-grids, and each sub-grid is assigned

to one processor of the parallel machine. The processors compute the wave fields on their sub-grids and share only the field values on the interfaces with their neighbors. The finite-difference model has been implemented to run both on a Cray T3E supercomputer with 544 processors (located at the ERDC Massively Shared Resource Center in Vicksburg, Miss.) and on a PC computer cluster located at the Georgia Institute of Technology. The PC cluster contains 50 Pentium III processors and has been especially built for this project.

3. INTERACTION OF ELASTIC WAVES WITH BURIED ANTIPERSONNEL MINES

The interaction of elastic waves with anti-personnel mines, buried in sand, is to be investigated. First, the propagation of a Rayleigh surface waves along the surface is compared as measured experimentally and as computed numerically. Then, the interaction of elastic waves with a single anti-personnel mine is described. Finally, three anti-personnel mines are buried in the ground together with some rocks and a wooden stick.

In the experiment, the mines are buried in a large sand-filled box. The properties of sand, together with the properties of plastic, air, rocks, and wood, are depicted in Table 1. Note that the shear wave speed in sand is assumed to be depth-dependent. Note also that wood is usually anisotropic, but is assumed to be isotropic to simplify the numerical model. This assumption is justified by considering the small dimensions of the wooden stick used here.

Table 1. Parameters used for finite-difference simulation.

Sand	Shear wave velocity	$c_{s,\text{sand}}$	(depth-dependent)
	Pressure wave velocity	$c_{p,\text{sand}}$	250 m/s
	Material density	ρ_{sand}	1400 kg/m^3
Plastic	Shear wave velocity	$c_{s,\text{plastic}}$	1100 m/s
	Pressure wave velocity	$c_{p,\text{plastic}}$	2700 m/s
	Material density	ρ_{plastic}	1200 kg/m^3
Air	Shear wave velocity	$c_{s,\text{air}}$	0 m/s
	Pressure wave velocity	$c_{p,\text{air}}$	330 m/s
	Material density	ρ_{air}	1.3 kg/m^3
Granite	Shear wave velocity	$c_{s,\text{granite}}$	3500 m/s
	Pressure wave velocity	$c_{p,\text{granite}}$	5500 m/s
	Material density	ρ_{granite}	4100 kg/m^3
Wood	Shear wave velocity	$c_{s,\text{wood}}$	100 m/s
	Pressure wave velocity	$c_{p,\text{wood}}$	300 m/s
	Material density	ρ_{wood}	650 kg/m^3

The space step for the numerical model is chosen to be $\Delta x = \Delta y = \Delta z = 0.5$ cm; the time step is $\Delta t = 11.54$ μs and, thus, fulfills the Courant condition (the necessary condition for stability of the finite-difference algorithm). The excitation has the shape of a Gaussian pulse. To be able to compare the numerical and experimental results, the transfer function of the system is determined in a post-processing step for each point in space and convolved with the transducer motion as measured in the experiment.

3.1. Surface Wave Dispersion

A Rayleigh surface wave is seen to disperse as it propagates along the surface of the ground. This effect has been observed experimentally[1,2] and is believed to be mainly due to the shear wave speed in sand increasing with depth. The pressure within the sand grows with depth, thus enhancing the cohesion between the grains of the sand. The

increased cohesion causes the medium to be stiffer and the shear wave speed to become larger. The shear wave speed as a function of depth is empirically found to be

$$c_s = 150\left(1 - \frac{3}{10z^{0.3}+5}\right) \text{ m/s}, \tag{14}$$

where z is the depths in meters. The depth profile is graphed in Fig. 2.

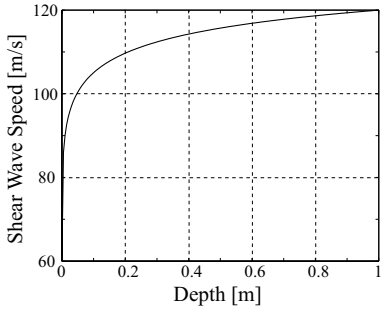

Figure 2. Shear-wave-speed depth profile.

Figure 3 shows waterfall graphs of the vertical particle displacement at the surface as measured experimentally (Fig. 3 (a)) and as determined numerically (Fig. 3 (b)). In these graphs, the displacement at a number of points along a straight line on the surface is plotted as a function of time and offset by the distance from the source. The slope of the traveling waves in the graph indicates the wave speed. Thus, by determining the slope, the different wave types can be distinguished.

Both in the experiment and in the numerical model, a pressure wave (P) and a Rayleigh surface wave (R) are seen to propagate. The pressure wave is faster than the Rayleigh wave and, thus, its slope is larger. The pressure wave is seen to decay quickly, due to the pressure wave being a volume wave rather than a surface wave. As the surface wave propagates, the pulse disperses and changes its shape. Dispersion arises, if wave components with different frequencies travel with different speeds. Due to the shear-wave speed increasing with depth, high-frequency components, which are more confined to the surface, will experience a lower shear-wave speed than low-frequency components, which reach deep into the ground. The agreement of experiment and numerical simulation is fairly good. The differences are mostly due to non-linear effects occurring in the sand. The non-linearities dampen the high-frequency components and, in this way, cause the pulse to broaden and to change in shape. By decreasing the amplitude of the excitation in the experiment, the agreement of experiment and numerical simulation can be improved. However, the signal-to-noise ratio of the radar output in the experiment will also decrease and, thus, the noise contents of the data will increase. Thus far, the non-linear effects are not incorporated into the numerical model.

Figure 4 shows the the vertical particle displacement on the surface and on a cross section through the ground at two times, T_1 and T_2, corresponding to the vertical lines in Fig. 3 (b). The wave fields have been computed numerically and are plotted on a logarithmic scale, in which black corresponds to the largest magnitude (0 dB) and white to the smallest (-60 dB). At T_1, a Rayleigh surface wave (R), a shear wave (S) and a pressure wave (P) are seen to propagate. The shear wave and the pressure wave are visisble only on the cross section through ground. The pressure wave induces head waves (H) as it propagates along the surface. Head waves are downwardly directed plane shear waves generated by the passage of bulk waves along the free surface. They usually decay rather quickly. Both the head waves and the surface wave are visible on the cross section and on the surface. At T_2, the waves have propagated farther. The pressure wave has left the range of the plot. The surface wave (R) and the shear wave (S) have separated. The head waves (H) have decayed and are not visible any more on the surface.

3.2. Interaction with a Buried Anti-Personnel Mine

To investigate the interactions with a buried land mine, a simple model for an anti-personnel mine is inserted into the numerical model. Figure 5 shows the simple model, together with a simplified cross-sectional drawing and a picture of a real TS-50 anti-personnel mine. The simple mine model consists of a main chamber containing plastic

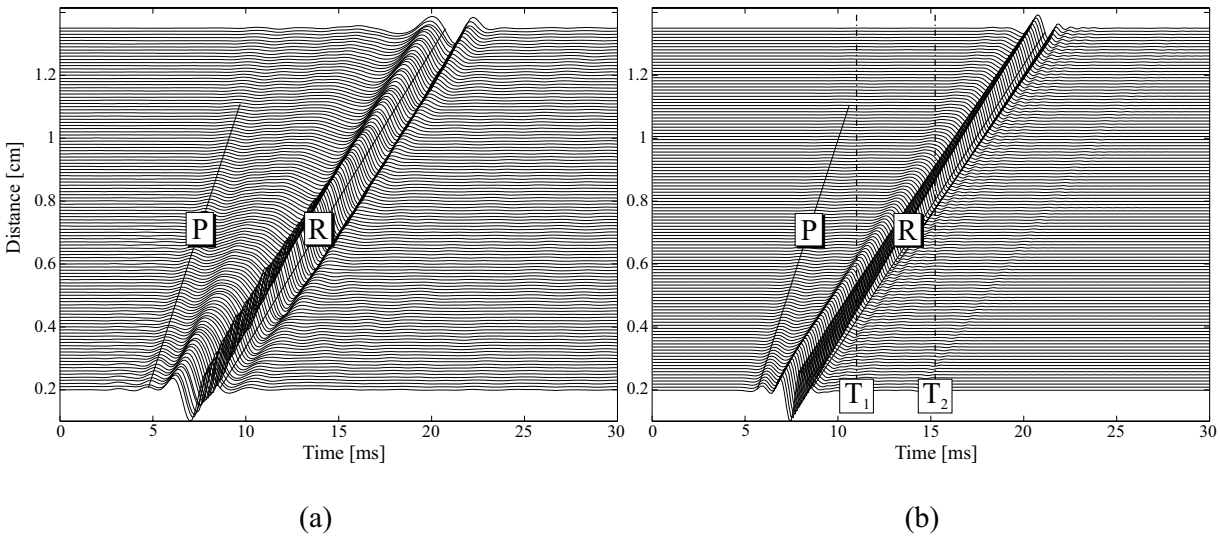

Figure 3. Waterfall graphs of the vertical particle displacement on the surface according to (a) experiment and (b) numerical simulation.

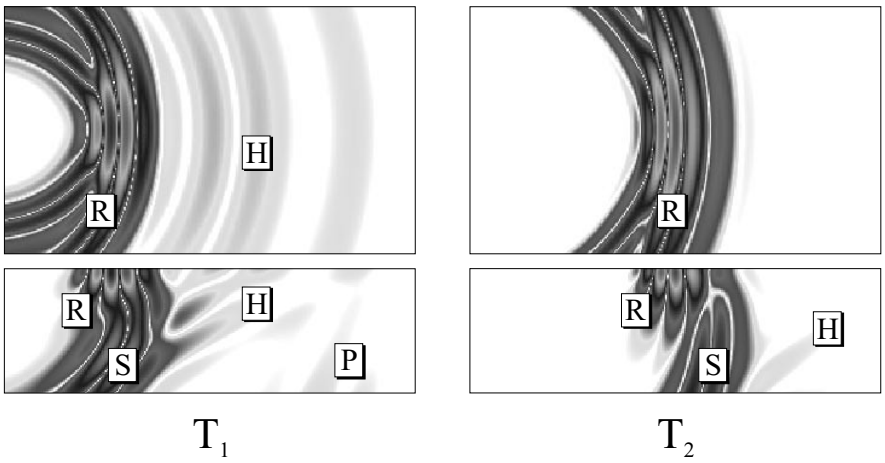

Figure 4. Normal particle displacement on the surface (top) and on a cross section through the ground (bottom). T_1 and T_2 correspond to the vertical lines in Fig. 3 (b).

explosives, and a smaller chamber on top of the mine's main chamber filled with air. In the cubic finite-difference grid, the round shape of the mine is approximated by cubes, leading to the stair-case form evident in Fig. 5. The air-filled chamber is inserted into the model to approximate the structure of a real TS-50 mine. A real TS-50 mine contains plastic explosives, a trigger mechanism, several chambers and is enclosed in a plastic case (see Fig. 5).

Figure 6 shows waterfall graphs of the mine-wave interaction for both experiment and numerical simulation. The mine is buried 2 cm beneath the surface, at a distance of 70 cm from the source. A pressure wave (P) and a Rayleigh surface wave (R) arise. The waves hit the mine and are reflected (rR) and transmitted. While the interaction of the mine with the pressure wave is weak, the surface wave strongly interacts with the mine. In both experiment and numerical simulation, resonant oscillations occur at the mine location and remain even after the waves have passed the mine. For the numerical model, it can be shown that the incident waves couple into flexural waves which arise in the thin soil layer above the mine.[4] These flexural waves are confined to the thin layer and form a standing wave pattern, giving rise to the resonant oscillations. While this explains the resonance in the numerical model, it gives only one possible cause for the resonance in the experiment. A real TS-50 mine has several chambers, it has a flexible case that can support both flexural and longitudinal waves, and it contains springs that can also give rise to resonances. The authors are currently working on refining the numerical model to incorporate more details of the mine.

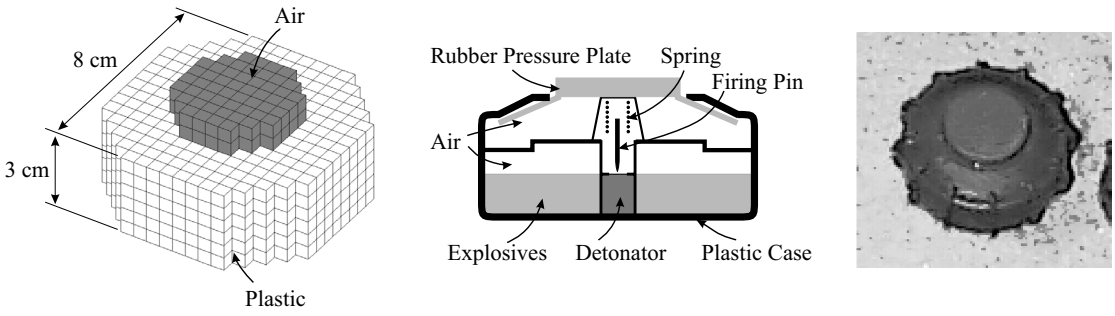

Figure 5. Simple model for the TS-50 anti-personnel mine; cross-sectional drawing and photograph of a real TS-50 mine.

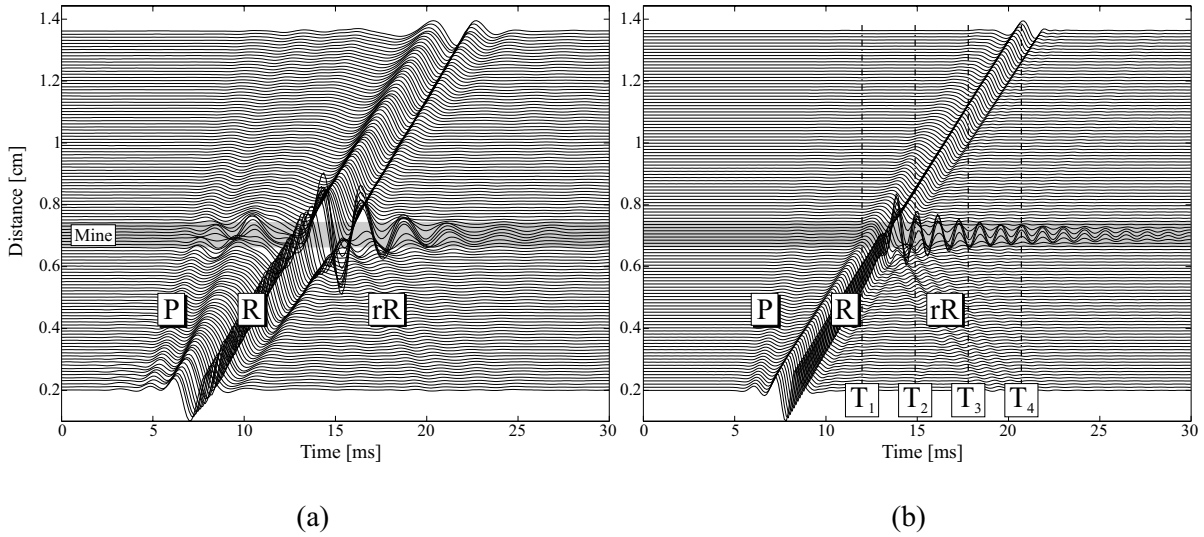

Figure 6. Interaction of elastic waves with a buried anti-personnel mine; waterfall graphs of the vertical particle displacement on the surface according to (a) experiment and (b) numerical simulation.

In Fig. 7, the vertical particle displacement on the surface and on a cross section through the ground is plotted. The fields are determined using the numerical model. The dynamic range of the plots is 50 dB. The wave fields are shown at four different instances in time, corresponding to the vertical lines marked with T_1, T_2, T_3 and T_4 in Fig. 6 (b). In the first plot, the surface wave is seen to just hit the mine. While only the surface wave (R) is visible on the surface, both the surface wave (R) and the shear wave (S) appear on the cross section. In the second plot, the surface wave has just passed the mine. The interaction of the surface wave with the mine gives rise to reflected surface waves (rR) and reflected shear waves (rS), which are clearly visible on the cross section. Pressure waves are also induced by the surface wave, but they are weak and not visible. In the third and fourth plot, the surface wave has passed the mine. Some energy, however, remains at the mine and causes the mine to vibrate and to radiate.

3.3. Mine-Wave Interaction in the Presence of Clutter

Next, it is investigated how the presence of clutter affects the mine-wave interaction. For this, three mines are buried in the ground together with a wooden stick and four rocks of various sizes and shapes. The material properties of the rocks (granite) and wood can be found in Table 1. Figure 8 shows how the mines, the rocks and the stick are arranged in the ground. The mine closest to the source is smaller (6 cm in diameter) than the other two mines (8 cm). The mines are buried 2 cm beneath the surface. The first mine lies at a distance of 50 cm from the source, the second at 70 cm and the third at 80 cm. The rocks and the wooden stick are located at different depth and have different shapes. The rock closest to the source is a tilted cuboid, the second rock is a sphere, and the other two consist of rectangular plates of random size. The wooden stick is modeled as a cylinder with a bent axis.

Figure 9 shows the vertical particle displacement on the surface in two series of pseudo color plots as obtained with the numerical model. The first series, Fig. 9 (a), has a dynamic range of 40 dB, whereas the second series,

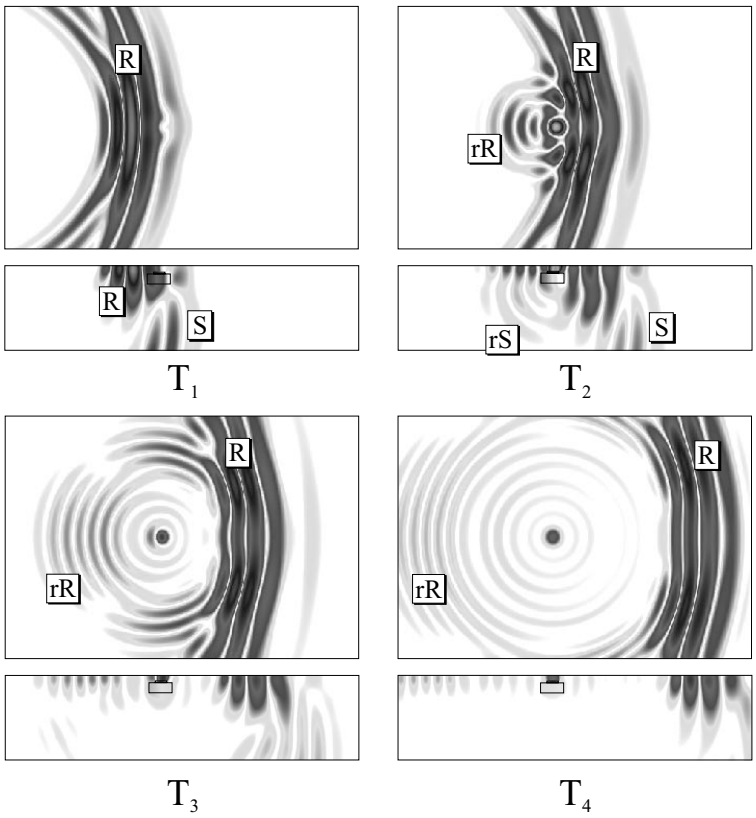

Figure 7. Interaction of elastic waves with a buried anti-personnel mine; pseudo color plots of the normal particle displacement on the surface (top) and on a cross section through the ground (bottom) at four instances in time, corresponding to the vertical lines in Fig. 6 (b).

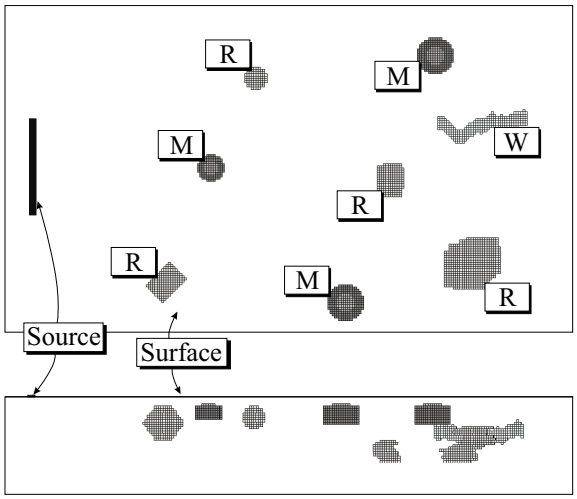

Figure 8. Three mines (M), 4 rocks (R) and a wooden stick (W) buried in the ground; top view and side view.

Fig. 9 (b), has a range of 70 dB. The dynamic range of the first series (40 dB) corresponds to the dynamic range of the experimental measurements. In the 70 dB range, however, more details of the wave-interaction with mines and clutter will be visible. In all plots, black represents the highest magnitude (0 dB) and white the lowest (-40 and -70 dB, respectively). The wave fields are shown at four instances in time.

At the first instance, i.e. the first row in Fig. 9, the surface wave just hits the mine closest to the source. In front

of the surface wave, head waves are propagating. The head waves decay quickly and, therefore, appear only at the earliest instance. On the 40 dB scale, only one faint head wave is visible. However, on the 70 dB scale, three head wave fronts are evident. These head waves have already reached the other two mines. At the second instance, the surface wave has passed the first and second mine and has just reached the third mine. A similar resonance to the one described in Sec. 3.2 is observed at the location of the first mine. Energy is trapped at the mine, and the mine radiates continuously. At the third and fourth time, the surface wave has passed all mines and all three are excited to resonant oscillations. The mines are clearly visible on the surface, whereas the rocks and the stick cannot be seen. The interaction with all rocks is rather weak. Very similar results have been observed also experimentally using real anti-personnel mines. Strong resonances could be seen at the mine locations, making it easily possible to distinguish the mines from the clutter.

4. CONCLUSIONS

A three-dimensional finite-difference model for elastic waves in the ground has been developed and implemented in a fully parallel fashion. Results are obtained and compared to experimental results. Experimentally, a Rayleigh surface wave is seen to disperse as it travels along the surface of the ground. This dispersion effect can be modeled also numerically by assuming a depth-dependent shear-wave speed profile. When an anti-personnel mine interacts with elastic waves, a strong resonance occurs at the mine location. This resonance has been observed in both experiment and numerical simulation. When clutter is present, this resonance can be used to distinguish mines from objects like rocks and wooden sticks, making it easy to locate the mines in the ground.

ACKNOWLEDGMENTS

This work is supported in part under the OSD MURI program by the US Army Research Office under contract DAAH04-96-1-0448, by a grant from the US Office of Naval Research under contract N00014-99-1-0995, and by an equipment grant from the Intel Corporation.

REFERENCES

1. W. R. Scott, Jr., C. T. Schröder, and J. S. Martin, "An acousto-electromagnetic sensor for locating land mines," in *Detection and Remediation Technologies for Mines and Minelike Targets III, Proc. SPIE*, vol. 3392, pp. 176–186, 1998.
2. W. R. Scott, Jr. and J. S. Martin, "Experimental investigation of the acousto-electromagnetic sensor for locating land mines," in *Detection and Remediation Technologies for Mines and Minelike Targets IV, Proc. SPIE*, 1999.
3. C. T. Schröder and W. R. Scott, Jr., "Finite-difference time-domain model for elastic waves in the ground," in *Detection and Remediation Technologies for Mines and Minelike Targets IV, Proc. SPIE*, 1999.
4. C. T. Schröder and W. R. Scott, Jr., "A finite-difference model to study the elastic-wave interactions with buried land mines," *IEEE Trans. on Geophysics and Remote Sensing* , to be published.
5. C. T. Schröder, *A Finite-Difference Model for Elastic Waves in the Ground*, Diploma Thesis, Technische Universität Braunschweig, 1999.
6. J. Virieux, "P-SV wave propagation in heterogenous media: Velocity-stress finite-difference method," *Geophysics* **51**, pp. 889–901, April 1986.
7. A. Tavlove, *Computational Electromagnetics: The Finite-Difference Time-Domain Method*, Artech House, 1995.
8. J.-P. Berenger, "A perfectly matched layer for the absorption of electromagnetic waves," *J. Comput. Physics* **114**, pp. 185–200, 1994.
9. W. C. Chew and Q. H. Liu, "Perfectly matched layer for elastodynamics; a new absorbing boundary condition," *J. Comput. Acoustics* **4**, pp. 341–359, 1996.

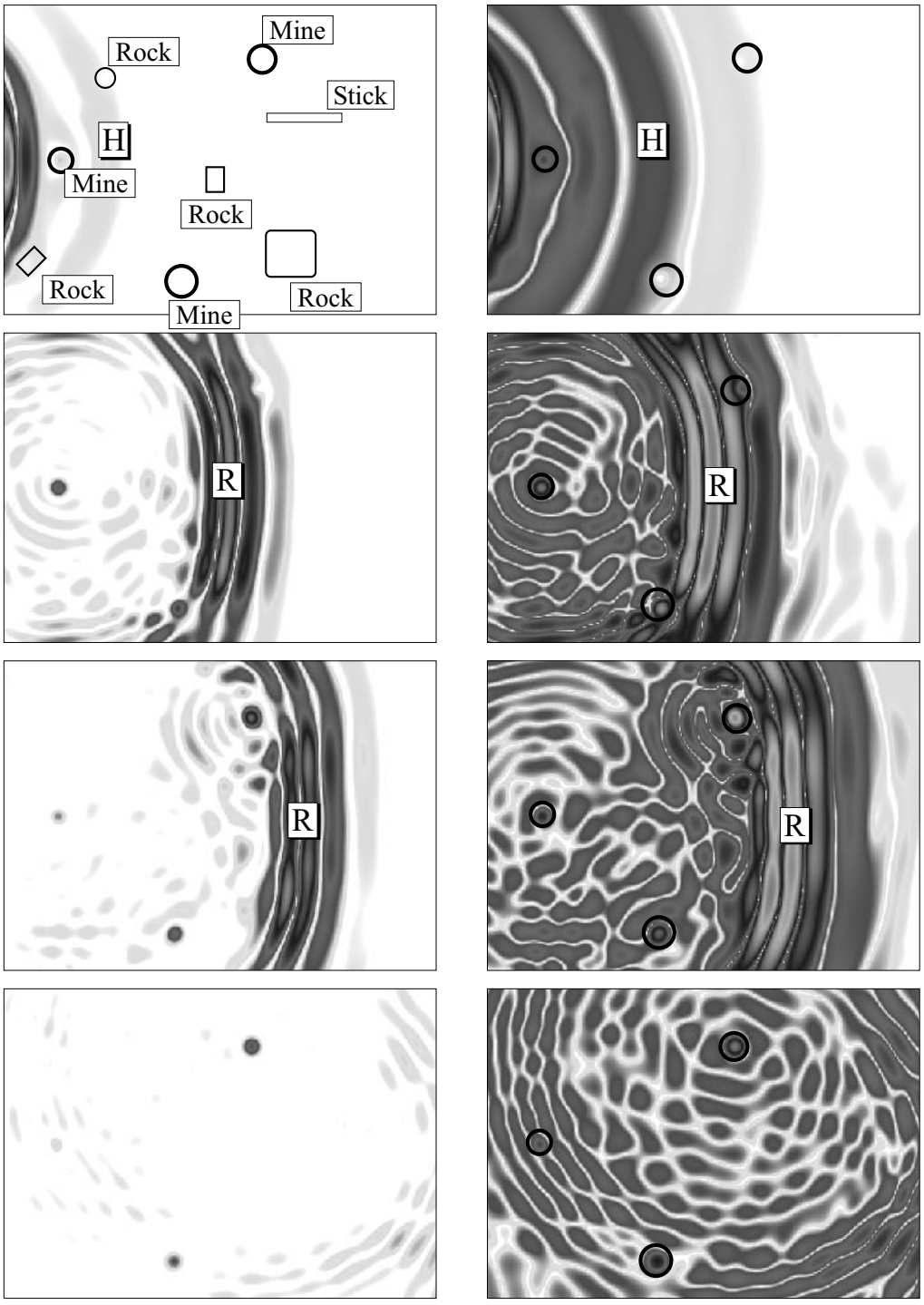

Figure 9. Three mines, 4 rocks and a wooden stick buried in the ground; pseudo color plots of the normal particle displacement on the surface with a dynamic range of (a) 40dB and (b) 70 dB.